

Optical Routing via High Efficiency Composite Acoustic Diffraction

Yuxiang Zhao^{1,*}, Jianguyong Hu¹, Ruijuan Liu¹, Ruochen Gao²,

Yiming Li¹, Xiao Zhang³, Huanfeng Zhu⁴, and Saijun Wu^{1†}

¹*Department of Physics, State Key Laboratory of Surface Physics and Key Laboratory of Micro and Nano Photonic Structures (Ministry of Education), Fudan University, Shanghai 200433, China.*

²*State Key Laboratory of Low Dimensional Quantum Physics,*

Department of Physics, Tsinghua University, Beijing 100084, China.

³*State Key Laboratory of Quantum Optics and Quantum Optics Devices, Institute of Laser Spectroscopy, Shanxi University, Taiyuan 030006, China. and*

⁴*State Key Laboratory of Modern Optical Instrumentation, College of Optical Science and Engineering, Zhejiang University, Hangzhou 310027, China.*

Acousto-optical modulation (AOM) is a powerful and widely used technique for rapidly controlling the frequency, phase, intensity, and direction of light. Based on Bragg diffraction, AOMs typically exhibit moderate diffraction efficiency, often less than 90% even for collimated inputs. In this work, we demonstrate that this efficiency can be significantly improved using a composite (CP) setup comprising a pair of 4-F-linked AOMs, enabling beamsplitting with fully tunable splitting amplitude and phase. The efficiency enhancement arises from two effects, termed "momentum echo" and "high-order rephasing," which can be simultaneously optimized by adjusting the relative distance between the two AOMs. This method is resource-efficient, does not require ultra-collimation, and maintains control bandwidth. Experimentally, we achieved a diffraction efficiency exceeding 99% (excluding insertion loss) and a 35 dB single-mode suppression of the 0th-order beam, demonstrating a full-contrast optical router with a switching time of less than 100 nanoseconds. Theoretically, we formulate the dynamics of CP-AOM in terms of multi-mode quantum control and discuss extensions beyond the $N = 2$ configuration presented in this work. The substantially enhanced performance of CP-AOMs, coupled with reduced acoustic amplitude requirements, may significantly advance our ability to accurately control light at high speeds with low-loss acousto-optics.

I. INTRODUCTION

From advanced quantum control [1–3] and optical quantum information processing [4–6] to the development of laser technology itself [7–9], accurate control of light with high enough speed is essential for enabling research advances at the frontiers. When the required control bandwidth exceeds a megahertz, mechanical control methods [10, 11] can be replaced by acousto-optical modulations (AOM) [12, 13] or electro-optical modulations (EOM) [14, 15]. While EOMs, based on electronic response, are ultrafast [2], the high voltage requirement for efficient operation [16] limits their applications in free space setups. When the control timescale is ten nanoseconds or longer [14], acousto-optical modulators become highly convenient for precisely controlling the phase, frequency, intensity, and propagation direction of light. Today, AOMs are ubiquitously used across fields, with applications ranging from ultrafast pulse shaping to quantum information processing.

The Bragg diffraction underlying AOM is a wave-mechanical effect well studied across fields. In ref. [17] an obvious link is highlighted between the paraxial acousto-optical modulation of light, and the time-domain diffraction of atomic matterwave using standing-wave pulses [18–22]. Benefited from time-domain pulse shaping

[23], Bragg diffraction techniques are under rapid developments [23–27] for achieving exceptional performances, even with uncollimated matterwave [23]. In contrast, in traditional AOM, even the first-order Bragg diffraction has a moderate efficiency, $R \sim 90\%$ at best in terms of optical power. In AOM, the acoustic field is designed by patterning the piezo transducer from the side [28, 29], not as versatile as time-domain pulse shaping for the matterwave control. The moderate efficiency limits the usefulness of the technique in applications where optical losses need to be suppressed, such as for photonic quantum information processing [4–6] or even just for multi-pass accumulation of AOM frequency-shifts [30]. Furthermore, since at these efficiencies the 0th-order has substantial residuals, traditional AOM can not be used as a router to divide the input beams into the 0th and the 1st orders on demand.

Inspired by the time-domain matterwave-control perfections [20, 23], one might anticipate exceptional AOM performance by engineering the acoustic field along the light propagation, *i.e.* along z in Fig. 1a within a single AOM [28]. But the field complexity is likely constrained by acoustic dynamics supportable by finite-sized AOM crystals. Instead, in ref. [17] we propose to precisely image arrays of AOMs to one another to coherently split Bragg-diffraction into an N -AOM process, thereby enhancing the controllability in a manner similar to composite-pulse quantum control [31, 32]. In ref. [17] the optimal control is discussed in terms of 2-mode dynamics. Experimentally, apart from the excep-

* yuxiangzhao21@m.fudan.edu.cn

† saijunwu@fudan.edu.cn

tional frequency-tuning range, the optical routing of high-repetition-rate ultrafast pulses, we also found that the achieved $R = 95\%$ efficiency was close to the limit set by high-order diffraction losses. Further improving R appeared to require either $N > 2$ AOMs, or, by keeping the $N = 2$ simplicity, to suppress the high-order losses by increasing the interaction distance L (Fig. 1a). For the latter case, we were facing a dilemma similar to that for the $N = 1$ traditional AOM (Sec. II D): The resonant interaction requires long distance L and large beam-size w , necessarily compromises the AOM control bandwidth $\Delta\omega_c \sim v_s/w$ set by the time for the sound wave to trespass the laser beam (Fig. 1a). In addition, the required large scale, uniform acoustic field could be difficult to generate technically.

In this work, we demonstrate that AOM efficiency can be perfected through composite diffraction in a resource-efficient manner without sacrificing control bandwidth. The key lies in exploiting wavefront reversal within the CP-AOM in a 4-F imaging setup (Fig. 1a). By precisely adjusting the position of the second AOM relative to the first (Fig. 1a), we achieve a remarkable diffraction efficiency of $R = 99.2\%$ for a weakly focused laser beam. At this high efficiency, the 0th-order output is effectively extinguished (Fig. 2c), and single-mode transmission is attenuated by over 35 dB. While our CP-AOM performance is currently limited by imaging aberrations, numerical simulations suggest that an efficiency of $R = 99.9\%$ is achievable with improved optical design. The unprecedented performance enables CP-AOM to function as a two-port beamsplitter with fast and fully tunable splitting amplitude and phase. The technique may be highly useful for advancements in laser physics and quantum optics. For example, the exceptional efficiency suggests applications such as efficient iterative frequency shifts to achieve multiple-GHz shifts [30], or rapid phase-tuning for the coherent combination of multiple CW [9] and pulsed [33, 34] lasers. Full-contrast modulation could be useful for tuning the group velocity of mode-locked laser pulses [8]. In quantum optics, using CP-AOM as a fully programmable optical router could enhance high-fidelity, high-speed shaping, and (de)multiplexing [17] of quantum light with AOM devices [4–6].

We note the diffraction efficiency of $R = 99.2\%$ demonstrated in this work excludes an insertion loss of approximately 5%, which can be significantly reduced by employing higher quality optics. To this end, the low RF-power requirements for driving CP-AOM can broaden the selection of acousto-optic materials, such as quartz-based AOMs [35], which are typically more challenging to drive but offer lower insertion loss.

In the following, we present our work in three sections. First, in Sec. II, we establish a minimal theoretical model to describe CP-AOM in terms of multi-mode quantum control, and present our numerical results using realistic AOM parameters on optimal diffraction with efficiency approaching $R = 99.9\%$. Next, in Sec. III, we present our experimental results, including the alignment method,

and discuss the performance of diffraction-optimized CP-AOM in detail. Finally, in Sec. IV, we discuss extension of this work on efficient realization of CP-AOM with single AOM, and on complex optical wavefront engineering with $N > 2$ AOMs. We then outline the prospects opened by the high-efficiency CP-AOM technique.

II. PRINCIPLES

Similar to multi-pulse optical control of matter waves [20, 23, 27, 36, 37], a paraxially propagating laser beam can be flexibly controlled by multiple acoustic diffractions using RF-driven AOM devices. In both scenarios, with collimated incidence, the diffracted waves often occupy only a few quantized diffraction orders. By truncating the associated Raman-Nath equations (Eq. (4)), the diffraction dynamics can be mapped to few-level quantum dynamics. As such, techniques in composite pulse quantum control [31, 32] can be utilized for precise and robust wavefront engineering with composite diffractions.

A. Raman-Nath equations

We first consider AOM₁ in the schematic setup in Fig. 1a. The incident light beam from left is diffracted by the RF-driven acoustic wave along \mathbf{e}_x inside AOM₁. By adjusting the orientation of the AOM, the Bragg-condition is met for efficient transfer of optical energy between the 0th and 1st orders.

We consider inside the AOM the index field is given by $n(\mathbf{r}, t) = \bar{n} + \delta n(\mathbf{r}, t)$, with

$$\delta n(\mathbf{r}, t) = \eta p \frac{\bar{n}^2 - 1}{2\bar{n}} \cos[k_s x - \omega_s t + \phi], \quad (1)$$

determined by the acoustic wave propagating along x . Here p is the photo-elastic coefficient [38]. ω_s is the angular frequency of the sound wave. The $\omega_s = v_s k_s$ relation is fixed by the speed of sound v_s in the AOM crystal. For simplicity we assume a step-function acoustic field, a constant acoustic amplitude $\eta(z) = \eta$ with uniform phase $\phi(z) = \phi$ within the interaction length $0 < z < L$. The acoustic amplitude and phase are controlled by $\{A_1, \varphi_1\}$, the amplitude and phase of the RF signal driving AOM₁ (Fig. 1a).

The optical field of the laser beam is written as $\mathbf{E}(\mathbf{r}, t) = \mathcal{E}(\mathbf{r}, t)e^{i(kz - \omega t)} + c.c.$. Here $k = \bar{n}k_0$ and $k_0 = \omega/c$. Paraxially, the Helmholtz equation for \mathbf{E} is reduced to that for the slowly-varying $\mathcal{E}(\mathbf{r}, t)$ envelop,

$$i(\partial_z + \frac{1}{v_{g,L}}\partial_t)\mathcal{E} = -\frac{1}{2k}\nabla_{\perp}^2\mathcal{E} - \delta nk_0\mathcal{E}. \quad (2)$$

Here $v_{g,L} \approx c/\bar{n}$ is the group velocity for the laser pulse. With the speed of sound to be much smaller than that for light, $v_s \ll v_{g,L}$, in the following analysis we ignore

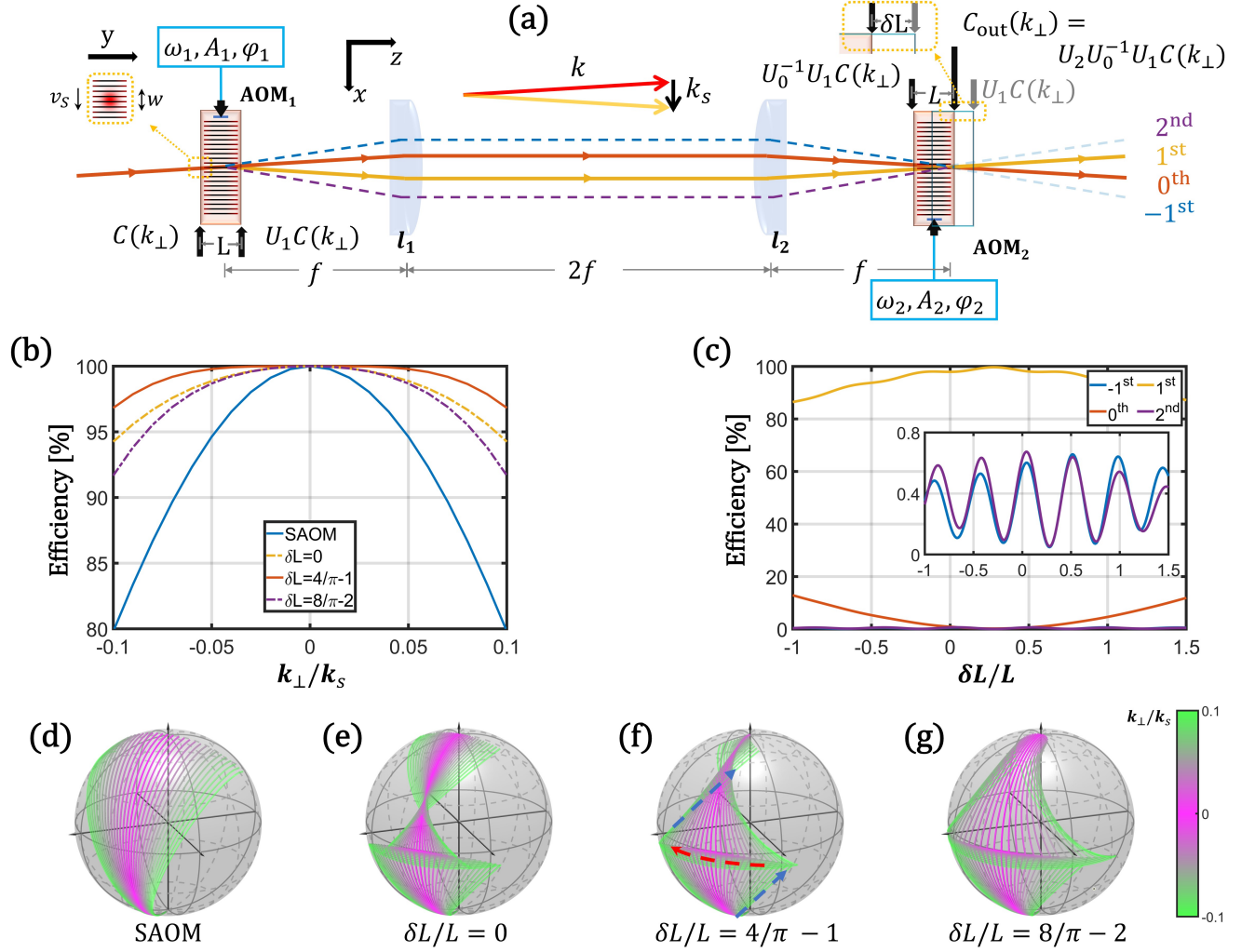


FIG. 1. CP-AOM with finely tuned inter-AOM distance δL to support ultra-high diffraction efficiency. (a): The setup and the associated wavefront evolution. We consider a collimated input beam from left with width w and wavevector spreading $\Delta k_{\perp} \approx 1/w \ll k_s$. The wavefront is represented by a $C(k_{\perp})$ -class to evolve according to Eqs. (3)(5). The AOM₂ is displaced from the perfect imaging plane to AOM₁ by δL . (b): $R(k_{\perp})$ vs k_{\perp} at different δL under 2-mode approximation. (c): Numerically simulated optimal diffraction efficiency (Eq. (8)) into the 1st order as a function of δL , together with the residuals in the 0th, 2nd and -1st orders. The inset gives the 2nd and -1st high-order losses. See Sec. II G for details. (d-g): Bloch sphere representation of diffraction dynamics (Eq. (10)) for single AOM (d), and for CP-AOM with various δL (e-g) as those in (b). The k_{\perp} is sampled between $-0.1k_s$ and $0.1k_s$ as those in (b). In (f) the dashed blue arrows represent $U_{1,2}$ diffractions. The dashed red arrow on the equator represents the U_0^{-1} “momentum echo”, for the example of $k_{\perp} = 0.1k_s$ trajectory.

the ∂_t -term in Eq. (2). We further drop out the y -index to specifically consider the diffraction along $\mathbf{k}_S = k_s \mathbf{e}_x$. To describe the spatially periodic interaction, we expand $\mathcal{E}(x, z)$ in the Bloch-wave basis for empty lattice,

$$\mathcal{E}(x, z) = \sum_n \int_{-k_s/2}^{k_s/2} C_n(k_{\perp}, z) e^{i((n-1/2)k_s + k_{\perp})x} dk_{\perp}. \quad (3)$$

The $C_n(k_{\perp}, z)$ is the amplitude of the n^{th} -order diffraction with quasi-momentum k_{\perp} . Here we choose to shift the Bloch basis by $\frac{1}{2}k_s$ to ensure the first-order Bragg resonance to meet between the $n = 0, 1$ orders for $k_{\perp} = 0$.

Physically, this requires the incident angle of the collimated laser beam to be tilted by the Bragg angle $\arcsin(k_s/2k_0)$ from \mathbf{e}_z to \mathbf{e}_x . With $K = \eta p \frac{\bar{n}^2 - 1}{\bar{n}} k_0$ to characterize the diffraction strength, the expansion leads to the coupled Raman-Nath equations,

$$i\partial_z C_n(k_{\perp}, z) = \frac{[(n - \frac{1}{2})k_s + k_{\perp}]^2}{2k} C_n(k_{\perp}, z) - \frac{K}{2} e^{i\phi} C_{n-1}(k_{\perp}, z) - \frac{K}{2} e^{-i\phi} C_{n+1}(k_{\perp}, z), \quad (4)$$

which can be rewritten as

$$i\partial_z C = (H_0(k_{\perp}) + V(K, \phi)) C. \quad (5)$$

The vector $C(k_\perp, z) \equiv (\dots, C_0, C_1, \dots)^T$ is referred to as the $C(k_\perp)$ -class in the following. The matrix elements $(H_0)_{mn} = \frac{[(n-1/2)k_s + k_\perp]^2}{2k} \delta_{m,n}$ and $V_{mn} = -\frac{1}{2}(K e^{i\phi} \delta_{m,n+1} + K e^{-i\phi} \delta_{m,n-1})$ are projections of the first and second terms on the right hand side of Eq. (2) to the Bloch-wave basis, respectively. We refer $(H_0)_{nn}$ as the propagation constant for the diffraction order n .

We formally integrate Eq. (5) to obtain the AOM₁ propagator for the $C(k_\perp)$ -class,

$$U(k_\perp; K_1, \phi_1) = e^{-i(H_0(k_\perp) + V(K_1, \phi_1))L}, \quad (6)$$

which is parametrized by the diffraction strength K_1 and acoustic phase ϕ_1 of the RF-controlled AOM₁ (Fig. 1a). For simplicity we assumed constant $K(z) = K_1$ and $\phi(z) = \phi_1$ according to Eq. (1). Practically the z -dependent interaction can be incorporated into the Eq. (6) integration in a straightforward manner.

Equation (5) conserves the quasi-momentum k_\perp . AOM diffraction of any input wavefront $\mathcal{E}(x, z)$ amounts to applying $U(k_\perp; K, \phi)$ in Eq. (6) to all the $C(k_\perp)$ -class, according to the Eq. (3) decomposition. The final wavefront control efficiency are averaged over k_\perp with Eq. (8) to be discussed shortly. As in Fig. 1a, to facilitate the discussions we use a specific $C(k_\perp)$ -class to represent the full wavefront, according to Eq. (3).

B. Composite diffraction

We now consider the full Fig. 1a setup where the AOM₁ output is imaged to AOM₂ for a second diffraction. We consider the 4-F system images the AOM₁ output to $z_2 = L + \delta L$, relative to the AOM₂ input plane which specifies $z' = 0$. Of course, the diffraction orders would already enter AOM₂ at $z' = 0$ before reaching $z' = z_2$. As being illustrated in Fig. 1a, the k_\perp -class of the input wavefront for AOM₂ can therefore be written as $C' = U_0^{-1} U_1 C(k_\perp)$ using the free-space propagator $U_0 = e^{-iH_0(L + \delta L)}$. With $U_c = U_2 U_0^{-1} U_1$, the AOM₂ output can be written as $C_{\text{out}} = U_c C(k_\perp)$. With $H_j = H_0(k_\perp) + V(K_j, \phi_j)$, the composite propagator for the $C(k_\perp)$ -class is

$$U_c(k_\perp; \{K_j, \phi_j\}, \delta L) = e^{-iH_2 L} e^{iH_0(L + \delta L)} e^{-iH_1 L}, \quad (7)$$

parametrized by the RF-controlled K_j, ϕ_j and the mechanically adjusted δL -distance.

C. Mode truncation

As in Fig 1a, we now consider collimated Gaussian beam incidence with $C_n(k_\perp) = f(k_\perp) \delta_{n,0}$, with a typical Gaussian profile $f(k_\perp) \propto e^{-k_\perp^2 w^2}$, $w \gg 1/k_s$. Our goal is to optimize the first-order Bragg diffraction efficiency,

$$R = \int dk_\perp R_1(k_\perp) f(k_\perp), \quad (8)$$

with $R_1(k_\perp) = |(U_c(k_\perp))_{01}|^2$ in the CP-AOM parameter space $\{K_1, \phi_1, K_2, \phi_2, \delta L\}$.

To simplify the analysis, Equation (5) can be truncated into a finite set of equations. Clearly, if we decide to only include $n = 1 - n_0, \dots, n_0$ orders, then the diffraction strength must be much smaller than the difference of propagation constants, $K \ll |H_{n_0 n_0} - H_{n_0 + 1 n_0 + 1}| \approx 2n_0 k_r$, so that the coupling between C_{n_0} and $C_{n_0 + 1}$ is inefficient. The associated high-order loss can be estimated with standard perturbation theory,

$$\mathcal{L}_{n_0}(K) \sim \frac{|C_{n_0}|^2 K^2}{16n_0^2 k_r^2} \quad (9)$$

in terms of intensity. Here $k_r = k_s^2/2k$ is a characteristic *diffraction constant*. The $|C_{n_0}|^2$ factor gives the average C_{n_0} population during AOM diffraction to support the $n_0 \leftrightarrow n_0 + 1$ coupling loss. Clearly, when $K \ll k_r$, $|C_{n_0}|^2$ decreases rapidly with n_0 .

The simplest truncation of Eq. (5) is to only include the $n = 0, 1$ orders with $n_0 = 1$ (see Eq. (13)). By parametrizing $C_0 = \cos(\frac{\Theta}{2}) e^{-i\Phi/2}$, $C_1 = \sin(\frac{\Theta}{2}) e^{i\Phi/2}$, the Bragg diffraction is mapped to 2-level ‘‘spin’’ dynamics [17] characterized by a state vector on the Bloch sphere $\mathbf{n} = (\sin\Theta \cos\Phi, \sin\Theta \sin\Phi, \cos\Theta)$ obeying

$$\dot{\mathbf{n}} = \mathbf{K} \times \mathbf{n}. \quad (10)$$

Here we define $\mathbf{K} = (K \cos\phi, K \sin\phi, \Delta)$ as a generalized spatial Rabi-vector. The mismatch $\Delta = k_s k_\perp / k$ is induced by the quasi-momentum k_\perp .

D. Simple AOM: \mathcal{L}_1 -loss and k_\perp -broadening

To understand efficiency constraints in simple AOM diffraction, we first replace the composite $U_c(k_\perp)$ for Eq. (8) with the simple $U(k_\perp; K_1, \phi_1)$ in Eq. (6). Full diffraction is designed within the 2-mode approximation by effectively setting $K_1 = \theta/L$ with $\theta = \pi$ so that $R(k_\perp = 0) = 1$. More precisely, for the diffraction of $C(k_\perp)$ -class, we have

$$R(k_\perp) \approx 1 - \mathcal{L}_1(K) - a_0 k_\perp^2 L^2. \quad (11)$$

The last term in Eq. (11) is the leading order correction of the $\theta = \pi$ -inversion by the k_\perp -mismatch. The coefficient $a_0 = (k_s/\pi k)^2$ is derived in Appendix A. Its effect to the 2-level dynamics is represented by the Bloch sphere dynamics in Fig. 1d. The diffraction efficiency $R(k_\perp)$ is represented by the solid blue curve in Fig. 1(b) within the 2-level model. With $K = \pi/L$, the $\mathcal{L}_1 \sim \pi^2/16k_r^2 L^2$ is the high-order diffraction loss according to Eqs. (9)(13).

Regarding the choice of the AOM interaction length L , Equation (11) suggests a trade-off between the \mathcal{L}_1 -loss and k_\perp -broadening effects. For incident laser beam with waist w (Fig. 1a) so that $\Delta k_\perp \approx 1/w$, an optimal diffraction efficiency with $1 - R \sim 1/k_s w$ can be reached with

$L = L_{\text{opt}} \sim \sqrt{w/k_r}$. To improve the optimal R requires increasing w and L^2 together. The wide- w diffraction over long distance L not only requires large-scale AOM fabrication, but also compromises the AOM control bandwidth $\Delta\omega_c = v_s/w$.

We note that the scaling for \mathcal{L}_1 -loss and k_{\perp} -broadening in Eq. (11) are derived assuming the step-function uniform acoustic field between $0 < z < L$ (Eq. (1)). While smoothing the rising and lowering edges of $\eta(z)$ tends to reduce \mathcal{L}_1 , as one expect to occur naturally in AOMs, such perturbations do not change the scaling for the optical control imperfections.

E. Momentum echo

We now consider optimization of Eq. (8) with the Fig. 1a $N = 2$ CP-AOM setup. First, as detailed in ref. [17], for CP-AOM it suffices to set $K_1 = K_2 = \theta/L$ with $\theta = \pi/2$. By adjusting $\phi_1 = \phi_2$, full inversion can be achieved at $k_{\perp} = 0$ within the 2-mode approximation. With $K = \pi/2L$, high-order diffraction loss for single AOM is suppressed by a factor of four, comparing to π -inversion, according to Eq. (9). With $R(k_{\perp} = 0) = 1$ optimized within the 2-mode approximation, we found that similar to Eq. (11), the efficiency for the composite diffraction of $C(k_{\perp})$ -class can be written as

$$R(k_{\perp}) \approx 1 - \mathcal{L}_c(K; \delta L) - a(\delta L)k_{\perp}^2 L^2 - b(\delta L)k_{\perp}^4 L^4. \quad (12)$$

The $\mathcal{L}_c(K; \delta L)$ term describes high-order diffraction loss as to be discussed shortly. For the k_{\perp} -broadening, here we include the 2nd and 4th-order $k_{\perp}L$ corrections. The coefficients $a(\delta L), b(\delta L)$ depend on the CP-AOM displacement δL (Fig. 1a). The expressions are given in Appendix A where we further show that $a(\delta L)$ is nullified at $\delta L_{\text{opt}} = (4/\pi - 1)L$ where $b = (4 - \pi)^2(k_s/\pi k)^4$. As such, the second order k_{\perp} -broadening is suppressed. In Fig. 1b we plot $R(k_{\perp})$ as a function of k_{\perp} . The Bloch sphere dynamics of the state vector \mathbf{n} , according to Eq. (10), are given in Fig. 1(d-g) for different choices of δL . The enhanced tolerance to k_{\perp} -broadening at the optimal δL_{opt} can be exploited to support efficient Bragg diffraction of small- w beams with accordingly enhanced control bandwidth.

The rephasing effect generated by $U_0^{-1} = e^{iH_0(L+\delta L)}$ is analogous to the spin echo used in nuclear magnetic resonance (NMR) to suppress inhomogeneous broadening [31]. As illustrated by the red dashed arrow in Fig. 1(f), the mismatch $\Delta = k_s k_{\perp}/k$ causes the state vector \mathbf{n} with different k_{\perp} to spread during U_1 . The U_0^{-1} operation, achieved through 4-F imaging, then reverses this spreading near the equator, setting the stage for the U_2 diffraction to complete the inversion. With a suitable choice of δL , the U_0^{-1} reversal is optimally deep to ensure a nearly perfect inversion by U_2 . We borrow the NMR concept to name the effect as a ‘‘momentum echo’’.

F. High-order rephasing

We now consider the $\mathcal{L}_c(K; \delta L)$ term in Eq. (12). For $K \ll k_r$ and with the $n = 0, 1$ truncation to Eq. (5), the \mathcal{L}_1 loss is primarily due to the off-resonant C_{-1}, C_2 -couplings. We evaluate the coupling loss by expanding the basis to $n = -1, 0, 1, 2$ orders into Eq. (5). The resulting 4-mode coupling equations can be simplified with a change of variables, $C_l^{\pm} = C_0 \pm C_1 e^{i\phi}$, $C_h^{\pm} = C_{-1} e^{-i\phi} \pm C_2 e^{2i\phi}$, for the $k_{\perp} = 0$ class, since both the $V(K, \phi)$ -coupling and the free $H_0(0)$ in Eq. (6) conserve the \pm sign symmetry. We focus on the $k_{\perp} = 0$ class in this section. Generally, with $|C_h^{\pm}|_{\text{in}} \ll |C_l^{\pm}|_{\text{in}}$ at the AOM incidence, the $V(K, \varphi)$ coupling leads to small shifts of C_h^{\pm} amplitudes, δC_h^{\pm} , that can be perturbatively evaluated to the leading K/k_r order as

$$\delta C_h^{\pm} \approx \frac{K(1 - e^{i2k_r L})}{4k_r} (C_l^{\pm})_{\text{in}}, \quad (13)$$

Again, here we assumed the step-function acoustic field specified in Eq. (1). The $\mathcal{L}_1(K) \sim |\delta C_h^{\pm}|^2$ is just the $n_0 = 1$ special example of Eq. (9). Practically the edge-smoothed acoustic field $\eta(z)$ (Eq. (1)) helps to reduce \mathcal{L}_c , but the K/k_r scaling is robust.

Clearly, the $2k_r$ difference in propagation constants in H_0 suppresses the couplings between C_l and C_h . In addition, for the $k_{\perp} = 0$ class, we have

$$\begin{aligned} C_l^{\pm}(z) &= C_l^{\pm}(0) e^{-i\frac{1}{4}k_r z}, \\ C_h^{\pm}(z) &= C_h^{\pm}(0) e^{-i\frac{9}{4}k_r z} \end{aligned} \quad (14)$$

during free propagation. Equations (13)(14) suggest the high-order loss for the CP-AOM setup takes the form

$$\mathcal{L}_c(K; \delta L) = \mathcal{L}_1(K) |\mathcal{A}_1 e^{i2k_r(L+\delta L)} + \mathcal{A}_2|^2. \quad (15)$$

Here $\mathcal{A}_{1,2} = O(1)$ are complex coefficients that depend on detailed diffraction dynamics in specific AOMs.

We refer the suppression of $\mathcal{L}_c(K; \delta L)$ in Eq. (12) at specific δL , according to Eq. (15), as a high-order rephasing effect. As illustrated in Fig. 1c, the suppression is achieved with a periodic array of optimal δL , which are decided by the phase factor $\phi_r = 2k_r(L + \delta L)$ as well as the phase angle of $\mathcal{A}_1/\mathcal{A}_2$. Of course, we hope the $(\mathcal{A}_1 e^{i2k_r(L+\delta L)} + \mathcal{A}_2)$ factor to be minimized at the δL_{opt} associated with Eq. (12), so that the high-order rephasing and the momentum echo described in the last section are optimized simultaneously (see the Fig. 1c example). Practically, with L itself fixed, the simultaneous optimization of the momentum echo and high-order rephasing effects can be achieved by finely adjusting $k_s = \omega_s/v_s$ and thus the diffraction constant k_r .

G. Numerical simulation

In Fig. 1c the momentum echo and high-order rephasing effects are illustrated with numerical simulation of

the full Eq. (4) that models the CP-AOM diffraction of a Gaussian beam at $\lambda = 780$ nm. The parameters in the simulation, $w = 185$ μm , $\omega_s = 2\pi \times 80$ MHz, $v_s = 4260$ m/s, $\bar{n} = 2.23$ for AOM based on TeO_2 crystal, are chosen according to the experimental setup to be introduced next. With the diffraction strength $K = \pi/2L \approx 0.09$ mm^{-1} , $K \ll k_r$ is well satisfied for $k_r = k_s^2/2k \approx 0.9$ mm^{-1} . Here, we choose the interaction length $L = 17$ mm for the square-shaped acoustic field. The value is close to the experimental estimation. In addition, it ensures $(\mathcal{A}_1 e^{i2k_r(L+\delta L)} + \mathcal{A}_2)$ is minimized at δL_{opt} . We emphasize that the same fine-tuning can be achieved with fixed L but varying $\omega_s = v_s k_s$, as suggested in the last section.

First, to illustrate the momentum echo, we compute the k_{\perp} -dependent diffraction efficiency $R(k_{\perp}) = |(C_{\text{out}})_1(k_{\perp})|^2$ under two-mode approximation, *i.e.*, with the $n = 0, 1$ truncation to Eq. (4) (Sec. II C). The initial condition is $C_n = \delta_{n,0}$. The results in Fig. 1b are obtained by integrating Eq. (4) for $U_1 C(k_{\perp})$ (blue line, Eq. (6)) and $U_c C(k_{\perp})$ (other lines, Eq. (7)). The advantage of choosing $\delta L = \delta L_{\text{opt}}$ is clearly seen with the red curve in Fig. 1b, where a nearly ideal $R(k_{\perp})$ is maintained under the two-mode approximation for $|k_{\perp}| < 0.05k_s$.

Next, we numerically integrate the full Eq. (4) for the Gaussian beam input, via Eq. (B1) as detailed in Appendix B, to obtain the k_{\perp} -averaged diffraction efficiency R according to Eq. (8). Losses to $n = -1, 2$ orders and the $n = 0$ residual are also recorded. The oscillatory $R_{-1,2}$ as a function of δL is with $2k_r$ frequency, according to Eq. (15). At $\delta L = \delta L_{\text{opt}}$, the $R_{-1,2}$ loss and the R_0 residual are simultaneously suppressed, leading to an optimal $R_{\text{opt}} = 99.7\%$. The losses to $n = -1, 2$ orders are blow 0.1%. The remaining 0.2% loss is primarily in the C_0 residual, as the momentum echo is not able to completely suppress the k_{\perp} -mismatch (Fig. 1f). By increasing w to 400 μm to reduce the incident k_{\perp} -spreading, $R_{\text{opt}} = 99.9\%$ is reached in the simulation. We performed additional simulations to verify that the simulated performance is robustly achievable with realistic AOM parameters and *improves further* for edge-smoothed acoustic amplitude $\eta(z)$.

Finally, without resorting to detailed derivations, in Appendix C we show numerically that $\mathcal{L}_c(K, \delta L)$, with δL_{opt} optimized at $K = \pi/2L$, decreases monotonically with K for $K \in [0, \pi/2L]$. The momentum echo is hardly affected by the reduced K either. Therefore, we expect nearly ideal performance of CP-AOM as a two-port beamsplitter with fully programmable diffraction efficiency and phase [17].

III. EXPERIMENTAL DEMONSTRATION

A. Setup and measurement procedure

The schematic of the CP-AOM setup is outlined in Fig. 1a. We use commercially available AOMs (G&H

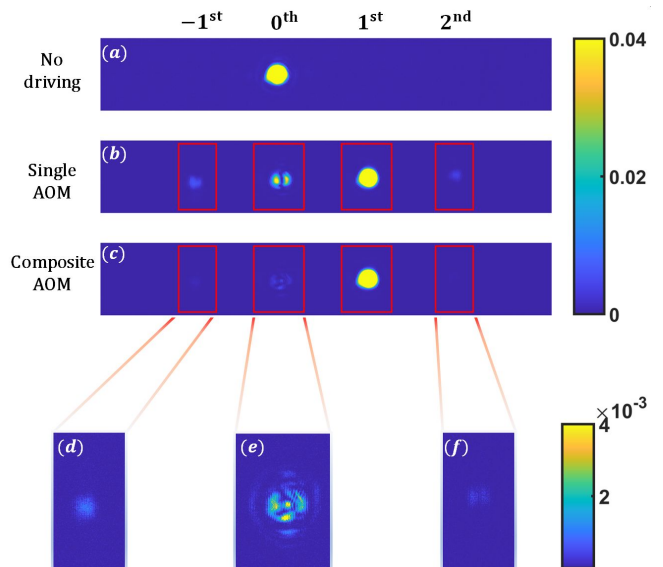


FIG. 2. Intensity profiles of the CP-AOM diffraction output, normalized by the peak intensity. (a): The 0th-order output with AOM_{1,2} off. (b): Output of optimal diffraction by AOM₁. (c-f): Output of optimal diffraction by CP-AOM.

3080-122) operating around the designed $\omega_s = 2\pi \times 80$ MHz frequency, driven by phase-coherent RF-signals from a multi-channel direct-digital synthesizer (Novatech 409B). The optical wavelength is $\lambda = 780$ nm. The Gaussian beam input for AOM₁ is collimated with a waist size of $w = 185$ μm ($1/e^2$ intensity). The AOM₁ output is imaged by a 4-F system to AOM₂. We choose a pair of $f = 100$ mm achromatic lenses (Thorlabs AC254-100-B) to ensure aberration-free 4-F links of the $n = -1, 0, 1, 2$ diffraction orders by AOM_{1,2}.

The CP-AOM output is detected by a scientific grade CMOS camera (Thorlabs CS165MU/M). The four output diffraction orders of interest, referred to as $I_n, n = -1, 0, 1, 2$ in Fig. 1a, are recorded by four areas on the camera sensor (Fig. 2) denoted as S_n in the following. Higher-order diffractions are also recorded. By substantially increasing the input laser power, we verified that the higher diffraction orders contribute negligible when CP-AOM operation is close to be optimal, and can hardly be detected ($< 0.01\%$ in power). These orders are therefore ignored in our following analysis. To retrieve Bragg-diffraction power efficiency R (Eq. (8)), twenty I_n measurements interleaved with background measurements are repeated and averaged. Typical background-subtracted and averaged images are displayed in Fig. 2. We obtain optical power $P_n = \sum_{S_n} I_n$ within each S_n . The Bragg diffraction power efficiency is then evaluated as $R = P_1 / \sum P_j$.

Clearly, accurate measurement of the diffraction efficiency R in our setup relies on a uniform and linear camera sensor response. By simultaneously measuring the laser power split into two paths, one with P_0 (AOMs off) by the camera and one by a calibrated power-meter

(Thorlabs S150C), we verify that the camera sensor read-out is highly linear when the incident laser power varies by 25 dB. Furthermore, to account for non-uniform camera sensitivity, we translate the motorized-stage mounted camera sensor along x and repeatedly measure P_0 (AOMs off) with different S_n . The relative responsivity ξ_n is found to deviate by up to 20% across the chip, primarily due to the sensor etalon effect. We apply the ξ_n correction to all the P_n measurements in the following. As the etalon effect is stable in our temperature-stabilized lab, we estimate this ξ_n correction to be accurate within 2% to impact negligibly the uncertainty of our $1 - R$ measurement in the following.

Finally, in addition to camera measurements, we use a flip mirror to couple the $n = 0, 1$ output orders into single-mode fibers when necessary. In static measurements, the single-mode outputs are monitored by the S150C power-meter. In transient measurements, we use a fast detector (Thorlabs PDA8GS) to evaluate the switching time of the CP-AOM.

B. Co-propagating geometry

In Fig. 1a, the diffractions by the 4-F-linked AOM_{1,2} share the same order number n with identical $\Delta\omega_n = n\omega_s$ frequency shifts. Consequently, the interference by the overlapping AOM_{1,2} orders are phase-stable. We refer this CP-AOM configuration as being with "co-propagating" acoustic fields.

The pairing of identical orders in Fig. 1a can be modified by reversing the direction of acoustic-wave propagation in AOM₂, as in our previous work [17]. From Eq. (1), the $x \rightarrow -x$ reversal is equivalent to the ω_s sign reversal. The overlapping diffraction by AOM_{1,2} therefore contains $\pm\omega_s$ sidebands. In our previous work [17], the resulting $2\omega_s$ interference is exploited for routing a synchronized mode-locked laser into the $n = 0, 1$ output directions. We refer that setup as CP-AOM in the "counter-propagating" geometry.

Evidently, with the light speed $v_{g,L} = c/n$ in Eq. (2) effectively set to infinity, the diffraction dynamics are determined by the instantaneous phases $\phi_j(t) = \phi_j(0) \pm \omega_s t$, $j = 1, 2$ for AOM_{1,2}, in both the co-propagating and counter-propagating geometries. In this work, we exploit the co-propagating geometry to demonstrate exceptional diffraction efficiency with a CW-laser input. Our conclusions are directly applicable to the counter-propagating geometry, enabling synchronized control of mode-locked laser pulses by sampling specific instances of $\phi_j(t)$ [17].

C. Optimizing CP-AOM

The procedure for optimizing the CP-AOM diffraction is similar to that in our previous work [17]. Within the 2-mode approximation, AOM_{1,2} serve as the first and second beamsplitters of a Mach-Zehnder interferometer,

respectively. The optimization process is thus aimed at maximizing the interferometric contrast. The observables during optimization are the $n = -1, 0, 1, 2$ output beams on the camera (Fig. 2). In this work, to enhance CP-AOM performance, particular attention is given to fine-tuning δL , the relative displacement between the AOM₂ output and the (imaged) AOM₁ output (Fig. 1a). The procedure is as follows.

First, AOM_{1,2} are switched on one by one. The diffraction strength for each AOM is adjusted with the RF-amplitudes $A_{1,2}$ to ensure moderate efficiency $R_{1,2} \leq 50\%$, *i.e.*, with intensities $I_1 \leq I_0$ observed on the camera. Then, by adjusting the orientation of AOM₂ relative to AOM₁, the $n = 1$ diffractions from AOM_{1,2} overlap as closely as possible on the camera.

Next, AOM_{1,2} are turned on simultaneously to enable diffraction interference. The RF frequency ω_1 is detuned from ω_2 by a small value, *e.g.*, $\delta\omega = 2\pi \times 0.5$ Hz, to scan the relative phase $\phi_{12} = \phi_1 - \phi_2$. Due to the interference, the linearly increasing ϕ_{12} leads to oscillatory $I_{0,1}$ output on the camera with $2\pi/\delta\omega$ periodicity. While the first-order diffractions from AOM_{1,2} overlap closely after the last step, any mode mismatch results in temporally varying $I_{1,2}$ distributions. To improve the mode-matching, the 3D location as well as the orientation of AOM_{1,2} are finely adjusted. This fine alignment results in uniformly interfering $I_{1,2}$ on the camera.

Finally, the RF amplitudes $A_{1,2}$ are finely adjusted to maximize the peak $R \propto P_1/\sum P_j$ during the $\delta\omega$ frequency scan. The peak R is recorded. The optimization is repeated as a function of the relative distance δL and then around the designed frequency ω_s if necessary. As such, the optimal R_{opt} is reached at a specific δL_{opt} , as expected from Fig. 1c.

D. Results

1. Optimal diffraction

A typical output of the optimal CP-AOM diffraction is shown in Fig. 2c. Compared to the AOM-off case in Fig. 2a, the 0th order appears simply shifted to the 1st order, despite the display being strongly saturated with the colorbar scaled to 4% of the peak I_n value. Closer inspection (Fig. 2(d-f)) indicates that the residual optical energy is split into $n = -1, 0, 2$ orders, with the dominant contribution from the irregularly-shaped I_0 residuals.

From Fig. 2c, a Bragg-diffraction efficiency of $R = 99.26\%$ is determined by analyzing I_n for $n = -1, 0, 1, 2$. Considering potential losses due to higher-order diffraction, the peak efficiency is estimated to be $R = 99.2\% \pm 0.1\%$. The optimal CP-AOM operation is remarkably stable over hours, due to common-mode rejection inherent to the 4-F setup against the vibrational and drifting noises. While the peak efficiency may degrade slightly over long time, it can be restored electronically, simply by adjusting the relative phase φ_{12} of the RF signals.

The exceptional CP-AOM performance is due to the momentum echo technique that suppresses the I_0 residual, and the high-order rephasing technique that suppresses the $I_{-1,2}$ losses. To highlight the difference made by CP-AOM, in Fig. 2b we provide the intensity image profiles for typical single-AOM diffraction. One clearly see much stronger losses in the $n = -1, 0, 2$ orders. Comparing to Fig 2e, the stronger I_0 residual is also simpler in shape. As discussed in Sec. II E, the k_{\perp} -mismatch leads to inefficient AOM diffraction. Conversely, efficient diffraction of sufficiently small k_{\perp} components serves as an effective mode-filtering process. Comparing to CP-AOM assisted by the momentum echo (Fig. 1f), efficient single-AOM diffraction can only occur within a much narrower k_{\perp} distribution (Fig. 1d).

Nevertheless, the $R = 99.2\%$ CP-AOM diffraction efficiency is still limited by the I_0 residuals as in Fig. 2e. The irregular I_0 suggests that the inefficient diffraction is caused by aberrations of 4-F imaging system in this work. The aberrations reduce the overlap between the AOM_{1,2} diffractions and therefore degrade the wavefront reversal (Eq. (7)). With more dedicated imaging optics, we expect further enhanced CP-AOM diffraction toward $R = 99.9\%$ as suggested by numerical simulations.

2. Frequency scan

As detailed in Ref. [17], CP-AOM enables efficient diffraction beyond the Bragg condition through quasi-phase-matching, where the acoustic-optical phase mismatches of AOM_{1,2} cancel each other. Here, after optimizing CP-AOM at the designed frequency of $\omega_s = 2\pi \times 80$ MHz, we shift ω_s to other values and optimize $R(\omega_s)$ electronically by adjusting the RF amplitudes $A_{1,2}$ and relative phase $\varphi_{12} = \varphi_1 - \varphi_2$. The optimal $\{A_{j,\text{opt}}(\omega_s), \varphi_{j,\text{opt}}(\omega_s)\}$ are saved as a parameter map, allowing us to select the carrier frequency ω_s of interest for driving CP-AOM while maintaining high diffraction efficiency $R(\omega_s)$.

The CP-AOM capacity for wideband operation is illustrated in Fig. 3a, which shows the RF-optimized efficiency $R(\omega_s)$ during a ω_s scan from 50 MHz to 100 MHz. For comparison, results from the same ω_s scan for single AOM_{1,2} are provided. Remarkably, quasi-phase-matching enables CP-AOM to achieve efficiency beyond 90% over a range of more than 30 MHz. As discussed in ref. [17], wideband modulation is highly valuable for CP-AOM to rapidly shift the phase, frequency [7], and output direction [13] of the first-order diffraction.

Efficient 1st-order diffraction is accompanied by effective extinction of the incident 0th-order beam. In Fig. 3b, we plot the I_0 rejection ratio, $\alpha = 10 \log(P_{0,\text{on}}/P_{0,\text{off}})$. Here, $P_{0,\text{off/on}}$ are the total power of I_0 recorded on the camera within S_0 (Fig. 2), measured when the optimal AOM operation is off and on, respectively. Similar to Fig. 3a, the attenuation data for the optimal CP-AOM and single-AOM are shown in Fig. 3b. The CP-

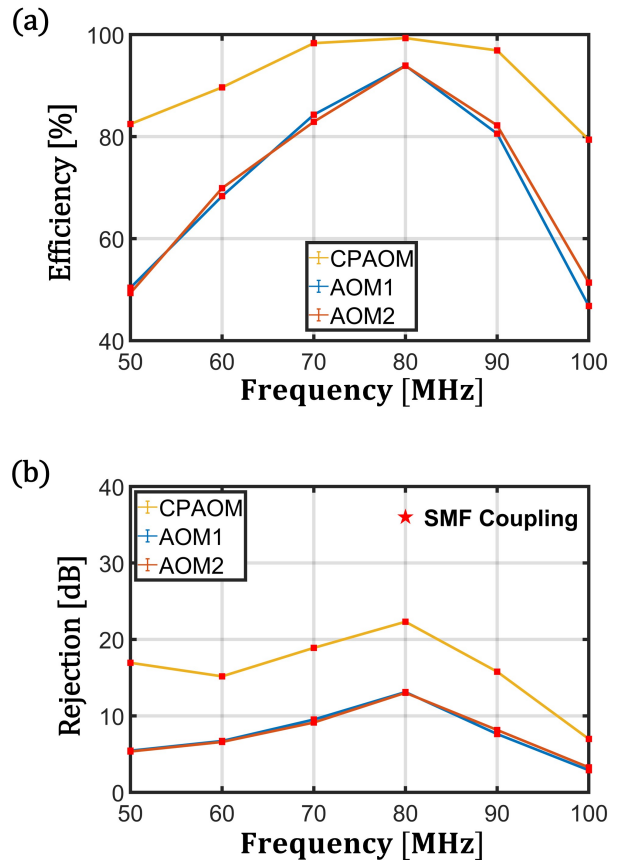


FIG. 3. Diffraction efficiency R (a) and I_0 rejection ratio α (b) as a function of the operation frequency ω_s of the CP-AOM aligned at 80 MHz. In (b) a star symbol suggests α_s obtained with single-mode fiber coupling (Sec. III D 3).

AOM achieves a remarkable $\alpha = 22$ dB attenuation at $\omega_s = 2\pi \times 80$ MHz, demonstrating its capability as a high-contrast two-port splitter in free space.

3. Single-mode attenuation

The I_0 residuals shown in Fig. 2(c,e) result from spatial-mode filtering by CP-AOM, displaying an irregular wavefront profile. By coupling the I_0 beam into a single-mode fiber, we expect to enhance the I_0 -rejection ratio further.

We couple both $I_{0,1}$ into single-mode fibers with coupling efficiencies of about 80% for both ports. When CP-AOM is switched on, the I_0 attenuation is found to be enhanced from the free-space value to $\alpha_s \approx 36$ dB. For comparison, the I_1 single-mode attenuation of ~ 50 dB is obtained when AOMs are switched off. Clearly, the single-mode I_0 rejection, which relies on the efficient Bragg-diffraction to remove the energy, is still limited by the I_0 residuals as those displayed in Fig. 2e. Nevertheless, the $\alpha_s > 35$ dB-level attenuation is typically sufficient in various applications.

4. Full contrast optical routing

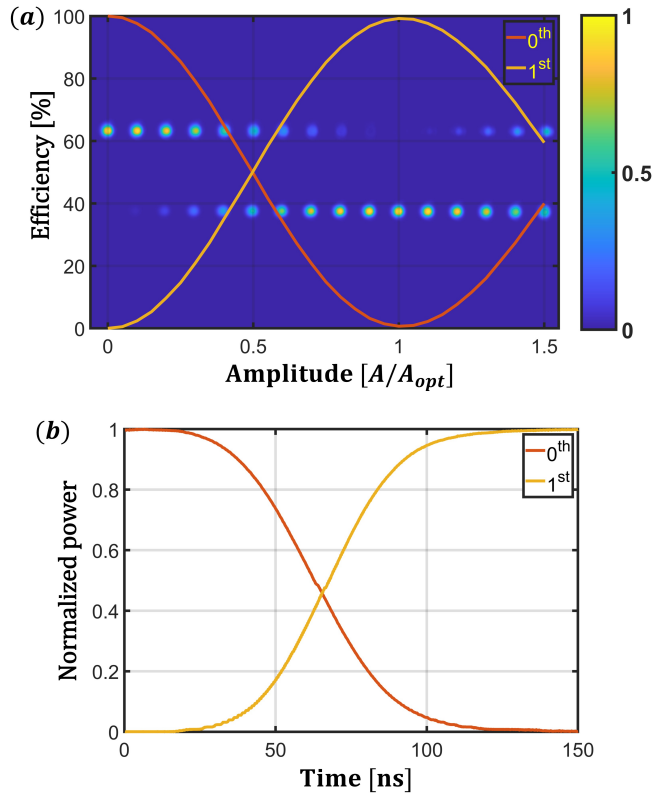


FIG. 4. CP-AOM as full contrast optical router. (a): The 1st-order diffraction efficiency R and 0th-order transmission efficiency T (excluding insertion loss) as a function of RF modulation amplitude A , evaluated from the intensity profile data as those in Fig. 2. Sixteen representative intensity profiles are selected as background, with the respective RF-amplitude A aligned to the x-axis. (b): The 0th and 1st-order output power during a nanosecond switch-on of CP-AOM.

We denote the RF-modulation amplitudes for the optimal CP-AOM diffraction in Fig. 2c as $A_{1,2} = a_{1,2}A_{\text{opt}}$, with $a_{1,2} \approx 1$ to be alignment-dependent relative amplitudes. As demonstrated in Fig. 4a, for $A_{1,2} = a_{1,2}A$ and by varying A between 0 and A_{opt} (thereby with K adjusted between 0 and $\pi/2L$, Appendix C), arbitrary division of optical power between the 0th and 1st diffraction orders can be achieved. In particular, by switching on/off CP-AOM, an incident beam is routed to the 1st/0th output diffraction order on-demand. While not shown, we note that when using CP-AOM, the optical phase for the 1st diffraction order output can be adjusted electronically with $\bar{\varphi} = (\varphi_1 + \varphi_2)/2$, a task that is difficult to realize with EOM-based fast optical routers [4–6].

To test the CP-AOM control speed, we simultaneously switch on the RF-signals driving AOM_{1,2} (Fig. 1a), and to measure the fiber-coupled $I_{0,1}$ outputs with the PDA8GS detector. To ensure synchronized switching of AOM_{1,2}, the time-of-arrival for the two TTL signals driv-

ing the CMOS switches (Analog Device ADG904 module) are relatively adjusted. As shown in Fig. 4b, with the switch-on the I_1 signal rises up from zero to the value associated with the $\sim 99\%$ efficiency, while the I_0 signal effectively falls to zero. Similar behavior is observed during the switch-off. A 10%-to-90% transient time of $\tau_s \approx 80$ ns is found in all cases. The transient time is consistent with the $w = 185$ μm beam size, and is similar to those achieved with the less-efficient single-AOM operations.

We note optical routing with $\tau_s \sim 80$ ns switching time is already useful for replacing EOMs to manipulate quantum light in various experiments [4–6]. Even faster CP-AOM control can be realized by using higher-frequency ω_s with a more focused laser beam, with a potential switching time down to 10 nanosecond level. On the other hand, when the requirement is to periodically route a periodic pulse train into two directions, then CP-AOM in counter-propagating geometry (Sec. III B) can be exploited for achieving GHz-level switching rate [17].

IV. DISCUSSIONS

The CP-AOM configuration in this work exploits high precision 4-F imaging optics to facilitate coherent double-diffraction by a pair of AOMs. The idea of optical imaging can be extended further to CP-AOM with $N = 1$, single-AOM and $N > 2$ multiple AOMs. The possibilities are discussed in the following.

A. Single AOM implementation

In the Fig. 1a setup, a mirror can be inserted in the middle plane of the 4-F system. Then, without AOM₂, the retro-reflection supports operation of CP-AOM with AOM₁ alone. We refer this way of operating CP-AOM as a Michelson-interferometer configuration. In this configuration, the relative phase ϕ_{12} between the double diffraction is time-dependent, $\phi_{12}(t) = 2\omega_s t + \phi_{12}(0)$, similar to CP-AOM in the counter-propagating geometry [17] (Sec. III B). Clearly, in the single-AOM operation half of the CP-AOM control degrees of freedom are lost. Nevertheless, as being discussed in ref. [17], the Michelson-CP-AOM can be particularly useful for controlling the repetition rate of mode-locked lasers.

Alternatively, one may replace AOM₂ with a retro-reflection mirror around the AOM₂-location where the diffraction orders from AOM₁ cross each other. The orders are reversed by the mirror reflection. Similar to the co-propagating CP-AOM explored in this work, the double-diffracted output orders are phase-stable. We refer this way of operating CP-AOM as a Sagnac-interferometer configuration. In this configuration, the relative phase ϕ_{12} is adjusted by the optical delay between the two acoustic diffractions, $\phi_{12} \approx 8\omega_s f/c$, which can be optimized by varying the distance between the two

imaging lenses ($l_{1,2}$ in Fig. 2a). Similar to the Michelson-CP-AOM, in the Sagnac-CP-AOM the number of AOM-control parameters are halved. Since ϕ_{12} cannot be electronically adjusted, the wideband operation as in Fig. 3 is not supported by the single-AOM operation.

We have constructed the single-AOM-based CP-AOM in the Michelson and Sagnac configurations to control the mode-locked [34] and CW lasers [39] in our lab. Depending on the type of AOM and operating ω_s , optimal diffraction efficiencies of $R > 97\%$ are regularly achieved.

B. Beyond 2-AOM

The CP-AOM with $N = 2$ as in Fig. 1a can be expanded to $N > 2$ using additional $4 - F$ imaging links. The $N > 2$ CP-AOM may support even more precise diffraction and potentially more optical control functionalities. Within the 2-mode approximation (Sec. II C), the possibility of enhancing the first-order Bragg diffraction with $N > 2$ has been discussed in ref. [17]. Beyond the analysis there, we note CP-AOM with $N > 2$ include additional $\delta L_j, j = 3, \dots, N$ translational degrees of freedom, similar to that is outlined in Fig. 1a, to further improve the CP-AOM performance. Furthermore, precise optical wavefront engineering appears feasible to enable efficient high-order Bragg diffraction or to generate symmetric output orders [20, 36]. The control degrees of freedom offered by the additional AOMs are useful resources to ensure multi-color beams controlled in a manner that is either sensitive or insensitive to the laser wavelength for *e.g.*, spatial-temporal shaping of ultrafast pulses [11].

Clearly, since the overall insertion loss in CP-AOM increases with N , a low insertion loss per AOM is particularly important for achieving the versatile CP-AOM functionality. To this end, we note that the N -AOM diffraction requires $\theta = \pi/N$ rotation (Eq. (10)) for achieving nearly ideal first-order Bragg diffraction. Therefore, increasing N drastically reduces [37] the RF-power requirement, $P_{\text{RF}} \propto 1/N^2$ for each daughter-AOM, for efficient acousto-optical modulation. This technical advantage may help wider application of quartz-based AOMs [35] that are typically more difficult to drive but support higher laser power and lower insertion loss.

C. Summary and outlook

Light sometime needs to be modulated to be useful. Acoustic-optical modulation, with the speed and accuracy, is a uniquely important technique for advancing optical science at frontiers. Inspired by advances of composite-pulse quantum control [20, 32], we demonstrate that AOM efficiency can be perfected by composite diffraction [17] in a resource-efficient manner without sacrificing the control bandwidth. This, combined with the versatile functionalities of CP-AOM (Sec. III B) [17] and the substantially reduced RF-power requirement

(Sec. IV B), may help to greatly expand our ability to accurately control light with low-loss acousto-optics.

Experimentally, the $R = 99.2\%$ diffraction efficiency achieved in this work with the $N = 2$ CP-AOM is likely limited by wavefront aberrations. More precise imaging optics would help to improve the efficiency further to the $R = 99.9\%$ level, thereby also enhancing the zeroth-order rejection ratio to beyond 40 dB (Fig. 3b). With improved optics and assuming 1% level insertion loss unrelated to diffractions, iterative application of CP-AOM would support $\Delta\omega = N_i\omega_s$ with $N_i \sim 100$, thereby pushing the free-space acousto-optical frequency-shifting range deeply into the microwave regime [30]. The low insertion loss combined with nearly ideal diffraction should also facilitate the application of CP-AOM as a fast two-port optical router for quantum light [4-6], or for coherently splitting/combining pulsed and CW lasers [8, 9, 17]. Similar to composite pulse quantum control [32], the CP-AOM functionalities expand in N -AOM systems with large N . Examples include achieving high-order Bragg diffraction [20, 36], general wavefront engineering [40], and spatial-temporal control of ultrafast pulses [11].

The CP-AOM technique discussed in this work is in direct analogy to composite pulse control of matter-wave [20, 36]. Nevertheless, a distinct feature in CP-AOM is the precise 4-F imaging for the effective wavefront reversal. Aided by developments of matterwave lensing techniques [41, 42], we also expect the momentum echo and high-order rephasing effects discussed in this work to be exploited in atom interferometry, to enhance the matterwave control efficiency/bandwidth [23, 27].

ACKNOWLEDGEMENTS

This work is supported by the National Key Research Program of China (Grant No. 2022YFA1404204), the National Natural Science Foundation of China (Grant No. 12074083), the Natural Science Foundation of Shanghai (Grant No. 23dz2260100), and the Shanghai Science and Technology Innovation Action Plan (Grant No. 24LZ1400300).

DISCLOSURES

The authors declare no conflicts of interest.

Appendix A: Derivation of Eqs. (11)(12)

We consider Eq. (6) under 2-mode approximation, and rewrite $H = H_0(k_\perp) + V(K, \phi)$ in terms of Pauli matrices,

$$H = \frac{1}{2}(\Delta\sigma_z - K\sigma_\phi). \quad (\text{A1})$$

Here $\sigma_x = (0, 1; 1, 0)$, $\sigma_y = (0, -i; i, 0)$, $\sigma_z = (1, 0; 0, -1)$, so that $\sigma_\phi = (0, e^{i\phi}; e^{-i\phi}, 0)$.

Single-AOM propagator according to Eq. (6) is:

$$U = \cos\left(\frac{\tilde{\theta}}{2}\right) - \frac{i\varepsilon}{\sqrt{1+\varepsilon^2}}\sin\left(\frac{\tilde{\theta}}{2}\right)\sigma_z - \frac{i}{\sqrt{1+\varepsilon^2}}\sin\left(\frac{\tilde{\theta}}{2}\right)\sigma_\phi \quad (\text{A2})$$

Here, for the collimated laser beam input, we introduce the small parameter $\varepsilon = \Delta/K$. For $K = \theta/L$, we further have $\varepsilon = \frac{k_s k_\perp L}{k}$. The actual rotation angle is accordingly expressed as $\tilde{\theta} = \sqrt{1+\varepsilon^2}\theta$.

With $L' = (L+\delta L)/2$, the free propagator U_0 is simply given by

$$U_0 = e^{-i\varepsilon KL'\sigma_z} \quad (\text{A3})$$

With $C_n(k_\perp) = \delta_{n,0}$ incidence, we focus on $R(k_\perp) = |U_{01}|^2$ with $U = U_1$ (single AOM) or $U = U_c$ (CP-AOM), as in the main text. For single AOM, it is easy to show that with $\theta = \pi$

$$R(k_\perp) = 1 - \left(\frac{k_s}{\pi k}\right)^2 (k_\perp L)^2 + \mathcal{O}(\varepsilon^4), \quad (\text{A4})$$

which leads to $a_0 = (k_s/\pi k)^2$ in Eq. (11).

Next, for $U_c = U_2 U_0^{-1} U_1$, we find

$$R(k_\perp) = \frac{4 \sin^2\left(\frac{\tilde{\theta}}{2}\right)}{1+\varepsilon^2} \times \left| \cos(\varepsilon KL') \cos\left(\frac{\tilde{\theta}}{2}\right) + \sin(\varepsilon KL') \frac{\varepsilon}{\sqrt{1+\varepsilon^2}} \sin\left(\frac{\tilde{\theta}}{2}\right) \right|^2 \quad (\text{A5})$$

We now consider $\theta = \pi/2$ [17], let $\delta = \delta L/L$, and expand Eq. (A5) to the fourth order in ε to obtain Eq. (12) in the main text, with

$$a(\delta L) = \left(\frac{\pi\delta + \pi - 4}{2}\right)^2 \left(\frac{k_s}{\pi k}\right)^2, \\ b(\delta L) = \left(\frac{\pi^4}{48}(1+\delta)^4 - \frac{\pi^3}{3}(1+\delta)^3 + (3 + 6\delta + 2\delta^2)\pi^2 - 12(1+\delta)\pi + 16\right) \left(\frac{k_s}{\pi k}\right)^4. \quad (\text{A6})$$

By setting $a(\delta L) = 0$, we find

$$\delta L_{\text{opt}} = \left(\frac{4}{\pi} - 1\right)L \quad (\text{A7})$$

leading to $b = (4-\pi)^2 (k_s/\pi k)^4$ in Eq. (12).

Appendix B: Numerical integration

The diffraction dynamics in CP-AOM is characterized by the U_c propagator in Eq. (7). Numerically, U_c is obtained by integrating either Eq. (2) or Eq. (4). The free-space propagator U_0 is obtained by setting $K = 0$ in these equations. To investigate the diffraction dynamics for a specific k_\perp component, we choose to integrate

Eq. (4) following proper mode truncation (Sec. II C). For example, the Fig. 1(b,d) illustrations are with $n_0 = 1$ to investigate the $n = 0, 1$ two-mode dynamics.

For a Gaussian beam input with continuous k_\perp distribution, such as for Fig. 1(c), we choose to directly integrate Eq. (2) with the incident Gaussian $\mathcal{E}(x, 0)$. With the ∂_t term ignored, Eq. (2) is rewritten as:

$$i\partial_z \mathcal{E}(x, z) = (H_0 + V(K, \phi))\mathcal{E}(x, z). \quad (\text{B1})$$

Here, $V(K, \phi) = -(\frac{K}{2}e^{i(k_s x + \phi)} + c.c.)$ and $H_0 = -\frac{1}{2k}\partial_x^2$ are equivalent to those in Eq. (4), but are expressed in the real x -space. Numerical integration of Eq. (B1) is carried out using a split-operator method [43], with small z -steps. The method alternates between diagonalizing the $V(K, \phi)$ term in real space and H_0 term in reciprocal space. To evaluate R in Eq. (8) for the Gaussian beam, according to Eq. (3), and more generally $R_n \equiv \int dk_\perp R_n(k_\perp) f(k_\perp)$ for the n^{th} -order output, we simply integrate the intensity of the output beam in the reciprocal k_x -space within $|k_x - nk_s| < k_s/2$.

Appendix C: High-order loss during partial splitting

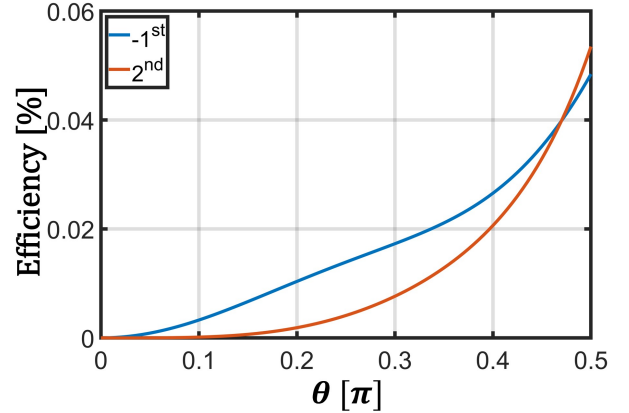


FIG. 5. The $n = -1, 2$ high-order loss as a function of θ for the Fig. 1a setup, at the optimal $\delta L_{\text{opt}} \approx 0.27L$ (Eq. (A7)) that minimizes the losses at $\theta = \pi/2$ according to Eqs. (12) (15), and Fig. 1c.

In Sec. II F we discussed optimal choices of δL to suppress high-order diffraction losses. As by Eq. (15), the optimal δL s that minimize \mathcal{L}_c loss depend on the complex coefficient $\mathcal{A}_{1,2}$, which are decided by AOM diffraction dynamics to be sensitive to K . A natural question arises, as whether the δL optimized at $K = \pi/2L$ remains efficient to suppress the high-order losses for varying K . A general analysis of $\mathcal{L}_c(K; \delta L_{\text{opt}})$ appears quite complicated. Instead, in Fig. 5 we provide a numerical example of the \mathcal{L}_c vs $K = \theta/2L$. Here $\delta L = \delta L_{\text{opt}}$ according to Eq. (A7) is optimized at $\theta = \pi/2$ as in Fig. 1c. We then numerically study the high-order loss as θ varies between

0 and $\pi/2$. The full-order simulation shares the same parameters as those for Fig. 1c. We find that the high-order losses decrease monotonically with K . Similar to Fig. 1c, we verified this observation to be stable when the acoustic field amplitude $\eta(z)$ modifies perturbatively in shape. Therefore, we expect the impact of high-order losses to be accordingly limited when using CP-AOM as

a programmable beamsplitter, as experimentally demonstrated with Fig. 4 in the main text.

-
- [1] J. Thom, G. Wilpers, E. Riis, and A. G. Sinclair, *Accurate and agile digital control of optical phase, amplitude and frequency for coherent atomic manipulation of atomic systems*, *Optics Express* **21**, 18712 (2013).
- [2] E. Torrontegui, D. Heinrich, M. I. Hussain, R. Blatt, and J. J. García-Ripoll, *Ultra-fast two-qubit ion gate using sequences of resonant pulses*, *New Journal of Physics* **22**, 103024 (2020), arXiv:2007.00734.
- [3] D. Bluvstein, S. J. Evered, A. A. Geim, S. H. Li, H. Zhou, T. Manovitz, S. Ebadi, M. Cain, M. Kalinowski, D. Hangleiter, J. P. Bonilla Ataides, N. Maskara, I. Cong, X. Gao, P. Sales Rodriguez, T. Karolyshyn, G. Semeghini, M. J. Gullans, M. Greiner, V. Vuletić, and M. D. Lukin, *Logical quantum processor based on reconfigurable atom arrays*, *Nature* **626**, 58–65 (2024), arXiv:2312.03982.
- [4] T. Rudolph, *Why i am optimistic about the silicon-photonics route to quantum computing*, *APL Photonics* **2**, 030901 (2017), arXiv:1607.08535.
- [5] L. S. Madsen, F. Laudenbach, M. F. Askarani, F. Rortais, T. Vincent, J. F. Bulmer, F. M. Miatto, L. Neuhaus, L. G. Helt, M. J. Collins, A. E. Lita, T. Gerrits, S. W. Nam, V. D. Vaidya, M. Menotti, I. Dhand, Z. Vernon, N. Quesada, and J. Lavoie, *Quantum computational advantage with a programmable photonic processor*, *Nature* **606**, 75–81 (2022).
- [6] S. Yu, Z. P. Zhong, Y. Fang, R. B. Patel, Q. P. Li, W. Liu, Z. Li, L. Xu, S. Sagona-Stophel, E. Mer, S. E. Thomas, Y. Meng, Z. P. Li, Y. Z. Yang, Z. A. Wang, N. J. Guo, W. H. Zhang, G. K. Tranmer, Y. Dong, Y. T. Wang, J. S. Tang, C. F. Li, I. A. Walmsley, and G. C. Guo, *A universal programmable Gaussian boson sampler for drug discovery*, *Nature Computational Science* **3**, 839–848 (2023), arXiv:2210.14877.
- [7] S. Koke, C. Grebing, H. Frei, A. Anderson, A. Assion, and G. Steinmeyer, *Direct frequency comb synthesis with arbitrary offset and shot-noise-limited phase noise*, *Nature Photonics* **4**, 462 (2010).
- [8] W. Hansel, M. Giunta, M. Fischer, M. Lezius, and R. Holzwarth, *Rapid electro-optic control of the carrier-envelope-offset frequency for ultra-low noise frequency combs*, *2017 Joint Conference of the European Frequency and Time Forum and IEEE International Frequency Control Symposium, EFTF/IFC 2017 - Proceedings*, 128–129 (2017).
- [9] D. Wang, Q. Du, T. Zhou, D. Li, and R. Wilcox, *Stabilization of the 81-channel coherent beam combination using machine learning*, *Optics Express* **29**, 5694 (2021).
- [10] P. Zupancic, P. M. Preiss, R. Ma, A. Lukin, M. Eric Tai, M. Rispoli, R. Islam, and M. Greiner, *Ultra-precise holographic beam shaping for microscopic quantum control*, *Optics Express* **24**, 13881 (2016), arXiv:1604.07653.
- [11] L. Chen, W. Zhu, P. Huo, J. Song, H. J. Lezec, T. Xu, and A. Agrawal, *Synthesizing ultrafast optical pulses with arbitrary spatiotemporal control*, *Science advances* **8**, eabq8314 (2022).
- [12] E. A. Donley, T. P. Heavner, F. Levi, M. O. Tataw, and S. R. Jefferts, *Double-pass acousto-optic modulator system*, *Review of Scientific Instruments* **76**, 063112 (2005).
- [13] D. Bluvstein, H. Levine, G. Semeghini, T. T. Wang, S. Ebadi, M. Kalinowski, A. Keesling, N. Maskara, H. Pichler, M. Greiner, V. Vuletić, and M. D. Lukin, *A quantum processor based on coherent transport of entangled atom arrays*, *Nature* **604**, 451–456 (2022), arXiv:2112.03923.
- [14] C. E. Rogers, III and P. L. Gould, *Nanosecond Pulse Shaping with Fiber-Based Electro-Optical Modulators and a Double-Pass Tapered Amplifier*, *Optics Express* **24**, 2596 (2015), arXiv:arXiv:1511.01228v1.
- [15] Y. He, L. Ji, Y. Wang, L. Qiu, J. Zhao, Y. Ma, X. Huang, S. Wu, and D. E. Chang, *Geometric control of collective spontaneous emission*, *Physical Review Letters* **125**, 213602 (2020), arXiv:1910.02289.
- [16] S.-w. Chiow, S. Herrmann, and S. Chu, *Nanosecond electro-optical switching with a repetition rate above 20 MHz.*, *Review of Scientific Instruments* **78**, 124702 (2007), arXiv:arXiv:0710.1374v2.
- [17] R. Liu, Y. Ma, L. Ji, L. Qiu, M. Ji, Z. Tao, and S. Wu, *Composite acousto-optical modulation*, *Optics Express* **30**, 27780 (2022), arXiv:2110.15537.
- [18] D. M. Giltner, R. W. McGowan, and S. A. Lee, *Atom interferometer based on bragg scattering from standing light waves*, *Physical Review Letters* **75**, 2638–2641 (1995).
- [19] Y.-J. Wang, D. Anderson, V. Bright, E. Cornell, Q. Diot, T. Kishimoto, M. Prentiss, R. Saravanan, S. Segal, and S. Wu, *Atom michelson interferometer on a chip using a Bose-Einstein condensate*, *Physical Review Letters* **94**, 090405 (2005).
- [20] S. Wu, Y.-J. Wang, Q. Diot, and M. Prentiss, *Splitting matter waves using an optimized standing-wave light-pulse sequence*, *Physical Review A* **71**, 043602 (2005).
- [21] S.-w. Chiow, Q. Long, S. Herrmann, and S. Chu, *Atom Interferometry with up to 24-Photon-Momentum-Transfer Beam Splitters*, *Physical Review Letters* **100**, 180405 (2008).
- [22] A. D. Cronin, J. Schemiedmayer, and D. Pritchard, *Atom Interferometers*, *Review of Modern Physics* **81**, 1051 (2008), arXiv:arXiv:0712.3703v1.
- [23] G. Louie, Z. Chen, T. Deshpande, and T. Kovachy, *Robust atom optics for Bragg atom interferometry*, *New Journal of Physics* **25**, 083017 (2023), arXiv:2303.16950.
- [24] R. H. Parker, C. Yu, B. Estey, W. Zhong, E. Huang,

- and M. Holger, *Controlling the multiport nature of Bragg diffraction in atom interferometry*, *Physical Review A* **94**, 053618 (2016).
- [25] B. Plotkin-Swing, D. Gochnauer, K. E. McAlpine, E. S. Cooper, A. O. Jamison, and S. Gupta, *Three-Path Atom Interferometry with Large Momentum Separation*, *Physical Review Letters* **121**, 133201 (2018), [arXiv:1712.06738](#).
- [26] P. Asenbaum, C. Overstreet, M. Kim, J. Curti, and M. A. Kasevich, *Atom-Interferometric Test of the Equivalence Principle at the 10-12 Level*, *Physical Review Letters* **125**, 191101 (2020).
- [27] J. N. Kirsten-Siemß, F. Fitzek, C. Schubert, E. M. Rasel, N. Gaaloul, and K. Hammerer, *Large-Momentum-Transfer Atom Interferometers with μ rad -Accuracy Using Bragg Diffraction*, *Physical Review Letters* **131**, 33602 (2023), [arXiv:2208.06647](#).
- [28] V. Balakshy, M. Kupreychik, S. Mantsevich, and V. Molchanov, *Acousto-optic cells with phased-array transducers and their application in systems of optical information processing*, *Materials* **14**, 451 (2021).
- [29] J. Wu, L. Liang, K. Tu, K. Li, and Z. Wang, *Serrated periodic electrode for high energy efficiency and large bandwidth acousto-optic modulators*, *Chinese Optics Letters* **21**, 031403 (2023).
- [30] C. Zhou, C. He, S. T. Yan, Y. H. Ji, L. Zhou, J. Wang, and M. S. Zhan, *Laser frequency shift up to 5 GHz with a high-efficiency 12-pass 350-MHz acousto-optic modulator*, *Review of Scientific Instruments* **91**, 033201-1 (2020).
- [31] M. H. Levitt, *Composite pulses*, *Progress in Nuclear Magnetic Resonance Spectroscopy* **18**, 61–122 (1986).
- [32] G. H. Low, T. J. Yoder, and I. L. Chuang, *Methodology of resonant equiangular composite quantum gates*, *Physical Review X* **6**, 041067 (2016), [arXiv:1603.03996](#).
- [33] A. Klenke, M. Muller, H. Stark, M. Kienel, C. Jau-regui, A. Tunnermann, and J. Limpert, *Coherent Beam Combination of Ultrafast Fiber Lasers*, *IEEE Journal of Selected Topics in Quantum Electronics* **24**, 0902709 (2018).
- [34] Y. Ma, X. Huang, X. Wang, L. Ji, Y. He, L. Qiu, J. Zhao, Y. Wang, and S. Wu, *Precise pulse shaping for quantum control of strong optical transitions*, *Optics Express* **28**, 17171 (2020), [arXiv:2004.05320](#).
- [35] Y. Vidne, M. Rosenbluh, and T. W. Hansch, *Pulse picking by phase-coherent additive pulse generation in an external cavity*, *Optics Letters* **28**, 2396 (2003).
- [36] K. J. Hughes, B. Deissler, J. H. T. Burke, and C. A. Sackett, *High-fidelity manipulation of a Bose-Einstein condensate using an optical standing wave*, *Physical Review A* **76**, 035601 (2007).
- [37] C. D. Herold, V. D. Vaidya, X. Li, S. L. Rolston, J. V. Porto, and M. Safronava, *Precision Measurement of Transition Matrix Elements via Light Shift Cancellation*, *Phys. Rev. Lett.* **109**, 243003 (2012).
- [38] A. Feldman, *Measurement of the Photoelastic Contents of Optical Materials*, *Optical Engineering* **17**, 453 (1978).
- [39] L. Ji, Y. He, Q. Cai, Z. Fang, Y. Wang, L. Qiu, L. Zhou, S. Wu, S. Grava, and D. E. Chang, *Superradiant Detection of Microscopic Optical Dipolar Interactions*, *Physical Review Letters* **131**, 253602 (2023), [arXiv:2101.10779](#).
- [40] M. C. Jabbari, C. Li, X. Liu, R. M. Córdova-Castro, B. Braverman, J. Upham, and R. W. Boyd, *Fast control of the transverse structure of a light beam using acousto-optic modulators*, [arXiv \(2024\)](#), [arXiv:2407.09675](#).
- [41] T. Kovachy, J. M. Hogan, A. Sugarbaker, S. M. Dickerson, C. A. Donnelly, C. Overstreet, and M. A. Kasevich, *Matter wave lensing to picokelvin temperatures*, *Physical Review Letters* **114**, 143004 (2015), [arXiv:1407.6995](#).
- [42] L. Asteria, H. P. Zahn, M. N. Kosch, K. Sengstock, and C. Weitenberg, *Quantum gas magnifier for sub-lattice-resolved imaging of 3D quantum systems*, *Nature* **599**, 571–575 (2021).
- [43] M. Suzuki, *Generalized Trotter's formula and systematic approximants of exponential operators and inner derivations with applications to many-body problems*, *Communications in Mathematical Physics* **51**, 183–190 (1976).